Dual-band Counter Circulary Polarized Radiation from a Single-arm Metamaterial-based Spiral Antenna

H. Nakano, *Life Fellow, IEEE*, J. Miyake, T. Sakurada, and J. Yamauchi, *Fellow, IEEE*

***Abstract*— A single-arm spiral antenna whose arm is made of a metamaterial (MTM) transmission line having right- and left-handed properties is discussed. This antenna, abbreviated as the 1-MTM-SPA, has an extremely low-profile structure (0.016 wavelength at a balanced frequency of 3 GHz) and does not need a balun circuit. It is predicted that the 1-MTM-SPA will operate as a circularly polarized (CP) antenna, where right-handed CP radiation is obtained within a particular frequency band and left-handed CP radiation is obtained within a different frequency band. Numerical analysis results obtained using two different techniques confirm the prediction for this dual-band counter-CP radiation. The 1-MTM SPA used for the confirmation shows an overlapping gain and axial ratio bandwidth of approximately 7%. The VSWR relative to the Bloch impedance value is less than two within the overlapping bandwidth, as desired. Experimental data are also presented.**

***Index Terms*—circularly polarized antenna, metamaterial transmission line, single-arm spiral antenna**

I. INTRODUCTION

A two-arm rectangular spiral antenna (2-RecSPA) is the counterpart of a two-arm round spiral antenna [1]. These spirals are considered wideband antennas [2]. Usually, the numerous straight filaments that constitute the 2-RecSPA are backed by a conducting plane (ground plane) to obtain a unidirectional beam. The 2-RecSPA is excited by a coaxial feed line with a balun circuit [3][4]. If the antenna size (peripheral length) of the 2-RecSPA [defined by four times the last arm filament length] is larger than one guided wavelength ($1\lambda_g$) of the current on the spiral arms, the radiation in the forward direction (let us assume this to be the positive z-direction) normal to the spiral plane (in the x-y plane) is circularly polarized (CP). Note that the rotational sense of this CP radiation is uniquely determined by the winding direction of the spiral arms; if the winding direction from the feed points (usually located at the center of the spiral) is in the counterclockwise direction, the CP radiation in the forward direction is right-handed (RH), and if the winding direction is in the clockwise direction, the CP radiation in the forward direction is left-handed (LH). It follows that the 2-RecSPA cannot radiate both LH- and RH-CP waves (counter-CP waves) in the forward direction, unlike a patch antenna, which has two ports fed with a 90^o phase difference to obtain counter-CP radiation [5]. Note that the counter-CP radiation from the patch is obtained at the same frequency, i.e., the patch operates as an element for single-band counter-CP radiation.

Recently, we investigated a modified 2-RecSPA [6] for obtaining *dual-band counter-CP radiation*, where right-handed CP radiation is obtained within a particular frequency band and left-handed CP radiation is obtained within a different frequency band. The arms of the antenna studied have a metamaterial (MTM) property, i.e., a left-handed property, together with a right-handed property [7]-[9]. It was found that the modified 2-RecSPA (referred to as the 2-RecSPA-Balance, or 2-MTM-SPA) can radiate dual-band counter-CP radiation. However, the 2-RecSPA-Balance has the limitation that it requires a balun circuit [3][4] for balanced mode excitation, resulting in increased complexity of antenna assembly and high fabrication cost.

This paper presents a novel spiral structure that does not use a balun circuit, thus overcoming the limitation of the 2-RecSPA-Balance. We investigate the operation of this spiral structure for dual-band counter-CP radiation. The investigation is performed using antenna parameters that would be typical of a realistic design. Note that the novel spiral is composed of a single strip arm having a metamaterial (MTM) property (double negative property [7]-[9]), and is denoted as the *1-MTM-SPA*. It should be emphasized that the arm of the 1-MTM-SPA is dispersive, and hence this paper examines moderately wideband antenna characteristics, not the extremely wideband antenna characteristics that are observed in conventional self-complementary spiral antennas [10][11].

Seven sections constitute this paper, where Section II describes the mechanism of LH CP radiation and RH CP radiation using a conventional spiral arm (continuous arm). Section III presents a novel spiral arm and its dispersion diagram, where the spiral arm is subdivided into numerous strip conductors. Based on the dispersion diagram, Section IV predicts that the 1-MTM-SPA will operate as an antenna for dual-band counter-CP radiation. In Section V, to confirm this prediction, numerical analysis results obtained by two different electromagnetic simulators [12][13] are presented. For further information, the antenna characteristics of the 1-MTM-SPA are compared with those of the modified 2-RecSPA [6]. Section VI presents an antenna fabrication example for the dual-band counter-CP radiation. Findings are summarized in Section VII.

Manuscript received February 29, 2012.

The authors are with Faculty of Science and Engineering, Hosei University, Koganei, Tokyo, 184-8584 Japan. Fax: 81-423-87-6183; (e-mail: nakano@ hosei.ac.jp).

II. Circularly Polarized Radiation

Fig. 1 shows a single-arm spiral antenna. The continuous straight strip filaments constituting the spiral arm have lengths L_1, L_2, …, L_M starting from the center. We assume that the current along the arm smoothly travels in only one direction, either from point T to point F (the coordinate origin) or from point F to point T, and that there is no reflected current.

First, we consider a situation where the current flows from point T to point F at frequency f_{LH}. This situation is designated as the TF case. We locate points A and B on the arm, both being on a straight line passing through the coordinate origin F and being quasi-point-symmetric with respect to point F [See Fig. 2(a)]. If the path length along the arm from point A to point B is $\lambda_g/2$ (with λ_g being the guided wavelength), then, the current elements at points A and B, illustrated by the arrows, are spatially in the same direction (i.e., the current elements are in phase), because of a 180° phase shift from point A to point B. As a result, the fields generated from these two current elements are added in the forward direction. The in-phase current elements travel along the arm near a square loop region of $1\lambda_g$ on the spiral plane, shown by a dotted line in Fig. 2(b), and hence the polarization of the resultant field is LH in the +z space.

Three facts are noted here: 1) current elements away from the $1\lambda_g$ square loop region make less of a contribution to the resultant field, because they are not in-phase; 2) the in-phase current elements are not located symmetrically with respect to the coordinate origin F due to the asymmetry of the spiral structure, and hence, the radiation is not exactly symmetric with respect to the z-axis; 3) the current experiences a *regressive phase shift* as it travels along the arm from point T to point F; conversely, the current experiences a *progressive phase shift* from point F to point T, i.e., the phase constant of the current along the arm, β, is negative with respect to the coordinate along the arm starting at point F and ending at point T (let us call this the *arm coordinate*).

Next, we consider a case where the current travels smoothly from point F to point T, opposite to the TF case. This is designated as the FT case. Fig. 3(a) shows a $1\lambda_g$ loop region at frequency f_{RH} ($\neq f_{LH}$), where points P and Q are quasi-point-symmetric with respect to the coordinate origin F. Like the TF case, the current element arrows at P and Q are spatially in-phase. These in-phase current elements rotate, producing CP radiation, whose rotational sense is RH in the forward direction. Note that the phase shift with respect to the arm coordinate (starting at point F and ending at point T along the arm, as already defined) is regressive, i.e., the phase constant β is positive with respect to the arm coordinate.

The aforementioned TF case (Fig. 2) is realized by locating the feed point at point T, while the FT case (Fig. 3) is realized by locating the feed point at point F. It follows that we need a switching circuit to select the feed point for counter-CP radiation; it is not possible for a spiral having a single *fixed* feed point to realize counter-CP radiation. In order for the spiral with a single fixed feed point to realize dual-band counter-CP radiation, the phase constant β with respect to the arm coordinate must have a negative value within a particular frequency band and a positive value within a different frequency band. Based on this requirement for the phase constant, we introduce a novel spiral arm in Section III.

III. MTM Spiral Arm

As shown in Fig. 4, the antenna arm shown in Fig. 1 is modified, fixing the feed point at the innermost point F. Each filament is composed of numerous strip conductors and is printed on a dielectric substrate (of thickness B and relative permittivity ε_r) backed by a conducting ground plane having an area of $s_x \times s_y$. The cell, defined by length p ($= 2p_0 + 2\Delta g$) and width w, has a conducting pin (radius ρ) extending toward the ground plane. The p is designed as the cell periodicity.

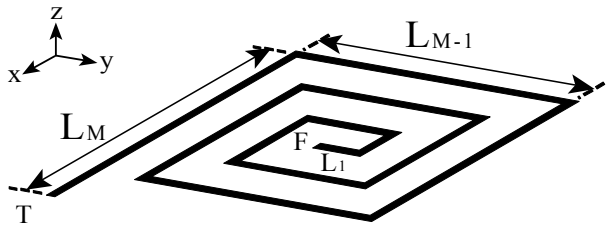

Fig. 1. Spiral antenna composed of a single continuous arm. The number of straight filaments is M, and the filament lengths are L_1, L_2, …L_{M-1}, L_M. The coordinate origin is denoted as F.

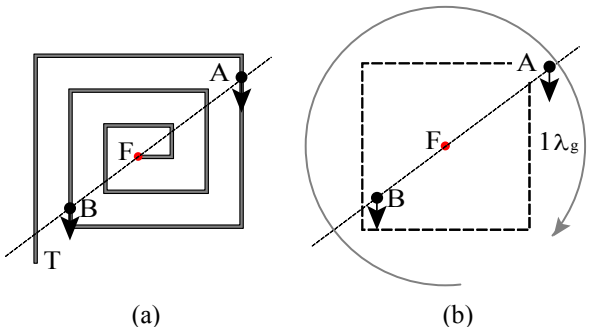

Fig. 2. TF case. (a) In-phase current elements. (b) LH CP radiation in the forward direction (z-direction). The length of the dotted ring line is one guided wavelength at frequency f_{LH}. The coordinate origin is denoted as F.

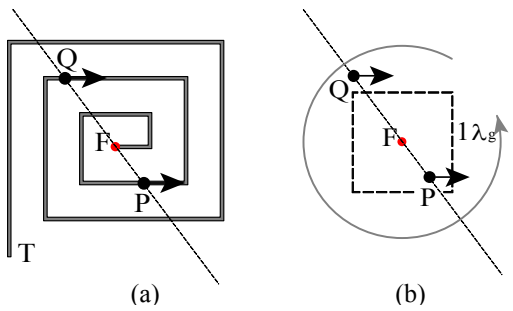

Fig.3. FT case. (a) In-phase current elements. (b) RH CP radiation in the forward direction. The length of the dotted ring line is one guided wavelength at frequency f_{RH}. The coordinate origin is denoted as F.

A shunt inductance L_L is inserted between the end of the pin and the ground plane and a capacitance C_L is inserted between neighboring arm conductors. Thus, the spiral arm has a metamaterial property (a left-handed property [6]-[9]) together with its inherent right-handed property. We abbreviate this single-arm metamaterial-based spiral antenna as the *1-MTM-SPA*. Note that the outermost point T is terminated with a Bloch impedance [14].

Fig. 5 shows the dispersion diagram for a unit cell, where β ($= 2\pi/\lambda_g$) is the phase constant of the current along the spiral arm, and k_0 ($= 2\pi/\lambda_0$, where λ_0 is the free-space wavelength) is the phase constant in free space. The lower and upper bound frequencies for a fast wave are marked by f_L and f_U, respectively, where $\beta/k_0 = -1$ at f_L and $\beta/k_0 = +1$ at f_U. The parameters used for this dispersion diagram are shown in Table I, leading to a balanced frequency of 3 GHz [7], which is denoted as $f_{balance}$. For a later comparison of the 1-MTM-SPA with the 2-MTM-SPA, the parameters in Table I are chosen to be the same as those used in [6]. Note that negative and positive phase constants for dual-band counter-CP radiation are prepared below and above $f_{balance}$, respectively. Also note that the cell periodicity p in Table I is chosen to be less than $\lambda_g/4$ across a fast-wave frequency band of f_L to f_U, taking into account the homogeneity condition of a composite right- and left-handed transmission line (CRLH TL) [8].

IV. N and H Frequencies and Prediction

A square loop of $1\lambda_g$ [see the dotted lines in Fig. 2(b) and Fig. 3(b)] acts as an *active region for CP radiation*. Therefore, the 1-MTM-SPA must have an area sufficiently large to support this active region. For this, it is required that the last filament length L_M be larger than $\lambda_g/4$ so that the antenna size (defined by peripheral length $C_{ant} = 4L_M$) is larger than $1\lambda_g$.

Fig. 6 shows the antenna size normalized to the guided wavelength, C_{ant}/λ_g, as a function of frequency, with the last filament length L_M as a parameter. A frequency that is below the balanced frequency and satisfies $C_{ant}/\lambda_g = 1$ is designated as the N frequency (f_N), and a frequency that is above the balanced frequency and satisfies $C_{ant}/\lambda_g = 1$ is designated as the H frequency (f_H). It is found that increasing the antenna size C_{ant} leads to a narrowing of the separation between f_N and f_H.

Based on the physical meanings of f_L, f_N, f_H, and f_U, the following four predictions are made: 1) the 1-MTM-SPA will exhibit maximum gain for LH CP radiation at a frequency between the lower bound frequency f_L and the N frequency f_N; 2) the 1-MTM-SPA will exhibit maximum gain for RH CP radiation at a frequency between the H frequency f_H and the upper bound frequency f_U; 3) as the frequency is increased from the N frequency toward the balanced frequency ($f_{balance}$ = 3 GHz), the gain for the LH CP radiation decreases, due to the disappearance of the active region for CP radiation, resulting from an increase in the guided wavelength; 4) conversely, as the frequency is decreased from the H frequency toward the balanced frequency $f_{balance}$, the gain for the RH CP radiation decreases, again due to the disappearance of the active region for CP radiation).

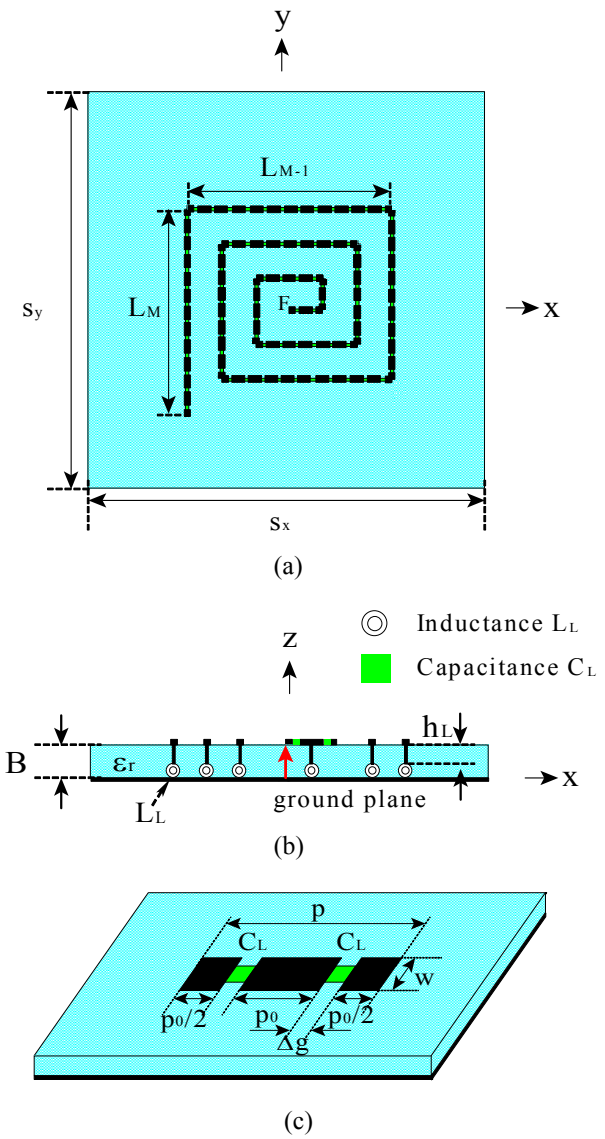

Fig. 4. Metamaterial-based single-arm spiral antenna (1-MTM-SPA). (a) Top view. (b) Side view. (c) Unit cell with inductance L_L and capacitance C_L loading.

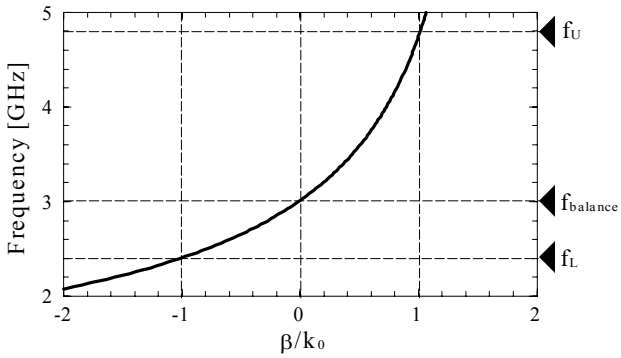

Fig. 5. Dispersion diagram for a unit cell. The notations f_L and f_U are the lower and upper bound frequencies for a fast wave, respectively.

V. Confirmation and Discussion

A. Confirmation of Predictions

For confirming the predictions made in Section IV, a 1-MTM-SPA is analyzed, where a small number of filaments (M =12) are used for the spiral arm to reduce the computation time. The filament lengths, $L_{2n-1} = L_{2n} = nL_1$ (n = 1, 2, …), are summarized in Table II, and result in an f_N = 2.7 GHz and f_H = 3.4 GHz (note: f_L= 2.4 GHz and f_U = 4.8 GHz from Fig. 5).

Fig. 7 shows the gain in the z-direction at frequencies below $f_{balance}$ = 3 GHz, which is obtained using the finite element method (FEM by Ansoft HFSS [12]). Note that G_L and G_R denote the gains for LH CP radiation and RH CP radiation, respectively [15]. These gains do not include the effect of input impedance mismatch. The actual gain is obtained by reducing the amount of input impedance mismatch from the G_L and G_R. For example, the amount of mismatch for VSWR = 2 is 0.51 dB. As predicted, the radiation at frequencies between the lower bound frequency f_L and the balanced frequency $f_{balance}$ is dominated by LH CP radiation (G_R is less than −10 dB and is not illustrated), and the maximum gain of G_L for LH CP radiation, G_{Lmax}, appears between the lower bound frequency f_L and the N frequency f_N.

The prediction that, as the frequency is increased from the N frequency f_N toward the balanced frequency $f_{balance}$ = 3 GHz, the gain G_L will decrease, is also confirmed. Note that this analysis result agrees with a result obtained using another technique [the finite integration technique (FIT) by CST MWS [13], illustrated by dots], therefore confirming the prediction made for LH CP radiation. The 3-dB gain reduction bandwidth for LH CP radiation in the z-direction, G_LBW, is calculated to be 9.6%.

Fig. 8 shows the gain in the z-direction at frequencies above $f_{balance}$ = 3 GHz. Again, as predicted, the maximum gain of G_R for RH CP radiation, G_{Rmax}, appears at a frequency between the upper bound frequency f_U and the H frequency f_H. In addition, the gain G_R decreases with decreasing frequency toward the balanced frequency $f_{balance}$. The analysis results obtained using the FEM and the FIT are in good agreement. The 3-dB gain reduction bandwidth for RH CP radiation in the z-direction, G_RBW, is calculated to be 9.7%. Thus, RH CP radiation above $f_{balance}$ is confirmed. As a result, our predicted dual-band counter-CP radiation (LH CP radiation within a particular frequency band and RH CP radiation within a different frequency band) is numerically confirmed.

B. Axial ratio, radiation pattern, and VSWR

Other antenna characteristics are presented in Figs. 9–11. Fig. 9 shows the axial ratio in the z-direction as a function of frequency. It is found that the 1-MTM-SPA has a moderately wide axial ratio bandwidth (ARBW). The bandwidth for a 3-dB axial ratio criterion for LH CP radiation, AR_LBW, is calculated to be 9.0%, while that for RH CP radiation, AR_RBW, is calculated to be 8.2%. Each axial ratio bandwidth is slightly larger than the overlapping frequency bandwidth (OBW) where a 3-dB axial ratio bandwidth and a 3-dB gain reduction bandwidth overlap: O_LBW = 7.0% [$\Delta f/f_{cent.}$ = (2.66 −2.48)/2.57] for LH CP radiation and O_RBW = 7.3% [$\Delta f/f_{cent.}$ = (3.68−3.42)/3.55] for RH CP radiation, shown by shaded regions in Fig. 9.

Table I. PARAMETERS

	Symbol	Value
Cell	ε_r	2.6
	B	1.6 mm
	w	2 mm
	p	10 mm
	p_0	4 mm
	Δg	1 mm
	ρ	0.5 mm
	h_L	0.6 mm
Ground plane	s_x	110 mm
	s_y	110 mm
LH elements	C_L	1.07 pF
	L_L	3.74 nH
Balanced frequency	$f_{balance}$	3.0 GHz

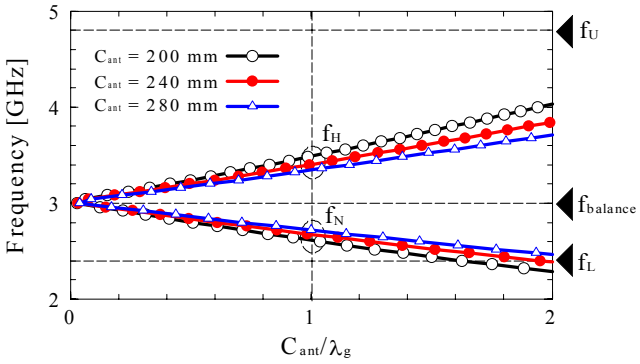

Fig. 6. Normalized antenna size C_{ant}/λ_g, where f_N and f_H denote the N and H frequencies, respectively, at which C_{ant}/λ_g = 1 is satisfied.

Table II. FILAMENT LENGTH

Symbol	Value
L_1	10 mm
L_2	10 mm
L_3	20 mm
L_4	20 mm
L_5	30 mm
L_6	30 mm
L_7	40 mm
L_8	40 mm
L_9	50 mm
L_{10}	50 mm
L_{11}	60 mm
L_{12}	60 mm

Fig. 10 depicts the radiation patterns within the overlapping bandwidths. The dashed (E_L) and solid (E_R) lines illustrate the LH CP and RH CP radiation field components, respectively. For confirmation, the radiation patterns at 2.6 GHz and 3.6 GHz are checked using FIT [13]; see the black dots for E_L and the white dots for E_R. It is found that the principal component E_L within the frequency band for LH CP radiation has a wider half-power beam-width (HPBW) than the principal component E_R within the frequency band for RH CP radiation. This is due to the fact that the $1\lambda_g$ active region (relative to the free-space wavelength λ_0) for LH CP radiation is smaller than that for RH CP radiation; $1\lambda_g/\lambda_0 = 1.67$ at 2.6 GHz for LH CP radiation and $1\lambda_g/\lambda_0 = 1.97$ at 3.6 GHz for RH CP radiation.

The radiation pattern is not perfectly symmetric with respect to the z-axis. If a perfectly symmetric radiation pattern is needed, a two-arm spiral structure in balanced mode is recommended. However, this will inevitably result in the increased cost of using a balun circuit, with the associated laborious circuit design.

The configuration parameters in Table I lead to a Bloch impedance of approximately 80 ohms. Fig 11 (a) shows the frequency response of the input impedance $Z_{in} = R_{in} + jX_{in}$, where R_{in} and X_{in} fluctuate in the vicinity of 80 ohms and zero ohm, respectively. The fluctuation is due to the subdivided arm and the arm bending. Based on this input impedance, the frequency response of the VSWR relative to 80 ohms ($VSWR_{80}$) is calculated and shown in Fig. 11 (b). The calculated results exhibit a $VSWR_{80}$ of less than 2 within a 7.0% overlapping bandwidth for LH CP radiation and a 7.3% overlapping bandwidth for RH CP radiation. Even if the VSWR is recalculated relative to 50 ohms ($VSWR_{50}$), it turns out not to exceed 2.2 for the overlapping bandwidths O_LBW and O_RBW, as desired.

C. Comparison between 1-MTM-SPA and 2-MTM-SPA

Next, we compare the antenna characteristics for the 1-MTM-SPA with those for a two-arm rectangular metamaterial-based spiral antenna (2-MTM-SPA) [6], where the 2-MTM-SPA is implemented using the same parameters shown in Table I. In contrast to the 1-MTM-SPA, the 2-MTM-SPA is fed using two feed lines with a 180-degree phase difference. Both MTM-SPAs have the same antenna size C_{ant} and the same antenna height B (= 1.6 mm). Table III shows a summary of the main characteristics of the 1-MTM-SPA and 2-MTM-SPA. It is found that the 1-MTM-SPA has a slightly larger radiation efficiency than the 2-MTM SPA, due to the fact that the total arm length of the straight filaments for the 1-MTM-SPA (420 mm) is longer than the unit arm length for the 2-MTM-SPA (210 mm). As a result, the 1-MTM-SPA has a slightly larger radiation efficiency than the 2-MTM-SPA, leading to slightly larger maximum gains G_{Lmax} and G_{Rmax} and hence slightly narrower gain bandwidths G_LBW and G_RBW. Note that the radiation efficiency for the 2-MTM-SPA equals the radiation efficiency of its unit arm. Also note that there is not a noticeable difference in the VSWR characteristics of the two MTM-SPAs.

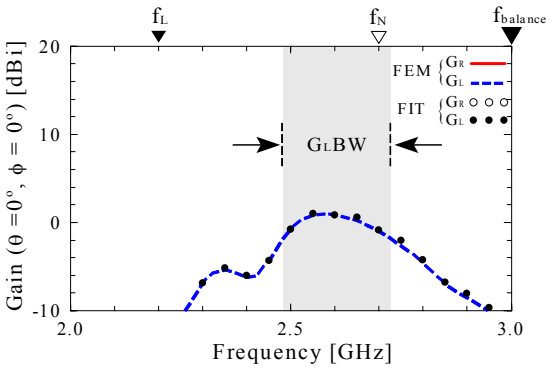

Fig. 7. Gain in the z-direction below $f_{balance}$ = 3 GHz. The LH CP radiation is dominant. G_LBW denotes a 3-dB gain reduction bandwidth for LH CP radiation. G_R is less than −10 dB and not illustrated. The analysis is performed using FEM [12] and FIT [13].

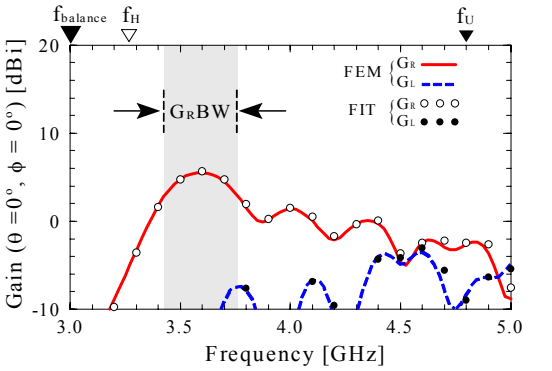

Fig. 8. Gain in the z-direction above $f_{balance}$ = 3 GHz. The RH CP radiation is dominant. G_RBW denotes a 3-dB gain reduction bandwidth for RH CP radiation. The analysis is performed using FEM [12] and FIT [13].

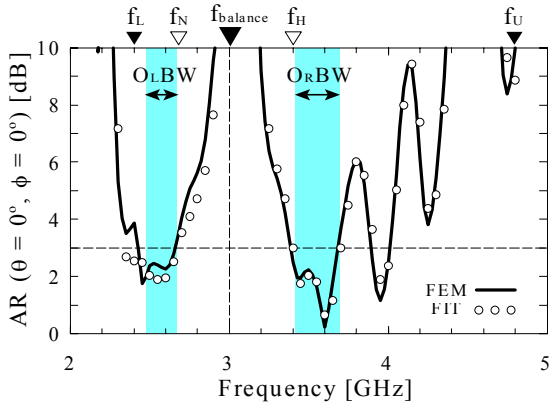

Fig. 9. Axial ratio in the z-direction as a function of frequency. Each shaded frequency region illustrates an overlapping frequency band, where the axial ratio bandwidth and the gain bandwidth overlap.

D. Change in the Ground Plane Size

The basic discussion for the 1-MTM-SPA is made in subsections A - C. Further detailed analysis is performed and discussed in the following subsections D - F. In this subsection D, we analyze the effect of the size of the ground plane, $s_x \times s_y$, on the antenna performance, where the ground plane has the same size as the dielectric substrate, $s_{x\text{-}sub} \times s_{y\text{-}sub}$, and is called the $G_{=S}$ ground plane [note that the ground plane throughout section III to section V A - C is a $G_{=S}$ ground plane of $s_x \times s_y = s_{x\text{-}sub} \times s_{y\text{-}sub} = 110$ mm $\times$ 110 mm]. The analysis reveals that, as the $G_{=S}$ ground plane size is decreased from $s_x \times s_y = 110$ mm $\times$ 110 mm, the back radiation increases. An example of this fact is depicted in Fig. 12, where the radiation pattern is calculated at an LP CP radiation frequency of 2.6 GHz and an RH CP radiation frequency of 3.6 GHz.

The analysis also reveals that the variation in the gain (in the z-direction) is small when the $G_{=S}$ ground is wider than 110 mm $\times$ 110 mm. [The gain G_L in the z-direction reaches a maximal value G_{Lmax} at a frequency near 2.6 GHz. The G_{Lmax} is changed from 0.9 dBi ($HPBW_{x\text{-}z\ plane} = 82^o$) at 110 mm $\times$ 110 mm to 0.6 dBi ($HPBW_{x\text{-}z\ plane} = 92^o$) at 127 mm $\times$ 127 mm; the gain G_R in the z-direction reaches a maximal value G_{Rmax} at a frequency near 3.6 GHz. The G_{Rmax} is changed from 5.5 dBi ($HPBW_{x\text{-}z\ plane} = 40^o$) at 110 mm $\times$ 110 mm to 5.6 dBi ($HPBW_{x\text{-}z\ plane} = 39^o$) at 127 mm $\times$ 127 mm.]

Based on these facts, we define the following values as the reference values: ground plane size $s_x \times s_y = 110$ mm $\times$ 110 mm $\equiv s_{x-ref} \times s_{y-ref}$, substrate size $s_{x-sub} \times s_{y-sub} = 110$ mm $\times$ 110 mm $\equiv s_{x-sub-ref} \times s_{y-sub-ref}$ ($= s_{x-ref} \times s_{y-ref}$), cell periodicity p = 10 mm $\equiv p_{ref}$, number of arm filaments M = 12 $\equiv M_{ref}$, $L_1 = 10$ mm $\equiv L_{1-ref}$, and antenna size $C_{ant} = 240$ mm $\equiv C_{ant\text{-}ref}$.

Next, we investigate the effect on the antenna performance when only the ground plane size $s_x \times s_y$ is increased from its reference value, holding the dielectric substrate size at its reference value; ($s_x \times s_y$, $s_{x-sub} \times s_{y-sub}$) = (varied, 110 mm $\times$ 110 mm). Note that the ground plane that is larger than the substrate is denoted as the *$G_{>S}$ ground plane* to distinguish it from the $G_{=S}$ ground plane. It is revealed that the variations in the antenna characteristics for a $G_{>S}$ ground plane of larger than the reference value $s_{x-ref} \times s_{y-ref}$ are relatively small. [As the ground plane size $s_x \times s_y$ is increased from the reference $s_{x-ref} \times s_{y-ref} = 110$ mm $\times$ 110 mm to 127 mm $\times$ 127 mm, the gain G_{Lmax} in the z-direction changes from 0.9 dBi ($HPBW_{x\text{-}z\ plane} = 82^o$) to 0.6 dBi ($HPBW_{x\text{-}z\ plane} = 94^o$) and the gain G_{Rmax} in the z-direction changes from 5.5 dBi ($HPBW_{x\text{-}z\ plane} = 40^o$) to 5.8.dBi ($HPBW_{x\text{-}z\ plane} = 39^o$). The radiation efficiencies η_{Lmax} for G_{Lmax} and η_{Rmax} for G_{Rmax} remain almost unchanged and are approximately 40% and 25%, respectively.

E. Change in Pitch

The distance between the centers of the adjacent spiral turns is defined as the *pitch*. The pitch for the spiral wound by filaments whose lengths are $L_{2n-1} = L_{2n}$ [mm] (n =1, 2,..., M) equals L_1 [mm]; that is, changing the pitch corresponds to changing the first filament length L_1.

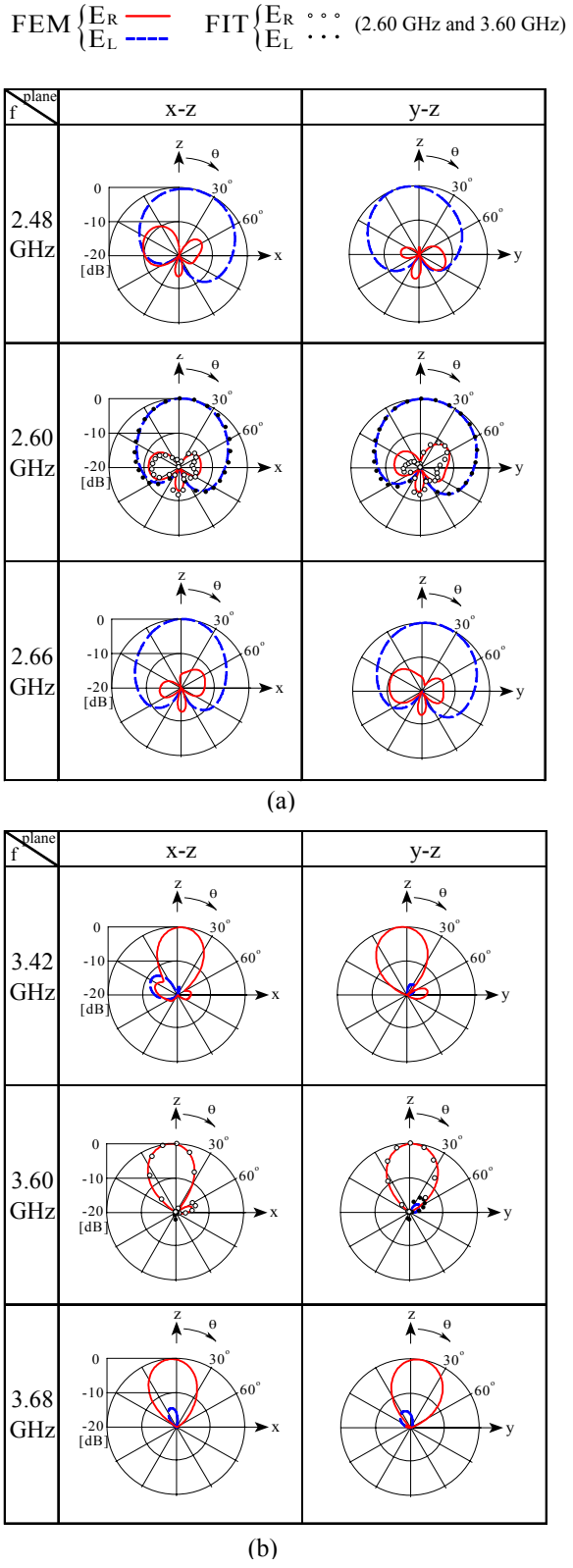

Fig. 10. Radiation patterns. (a) At frequencies within the overlapping band width O_LBW. (b) At frequencies within the overlapping band width O_RBW. FEM results at f = 2.6 GHz and 3.6 GHz are confirmed by FIT results.

In the following discussion, we change the pitch (equals L_1 [mm]). In response to this change, we choose the cell length (i.e., the cell periodicity p [mm]) to be L_1 [mm] and change the C_L and L_L in Table I to $(p_{ref}/L_1)C_L$ and $(p_{ref}/L_1)L_L$, in order not to change the dispersion diagram shown in Fig. 5. Note that the first filament is made of one cell of length p [mm]. Also, note that the first filament length, pitch, and cell periodicity change with the same value.

When L_1 is decreased under the condition that the antenna size ($C_{ant} = 4L_M$, where L_M is the longest/last filament length) is fixed, the number of arm filaments, M (which is as a function of L_1), increases and the total arm length $L_1 + L_2 + \ldots + L_M$ increases. This will lead to an increase in the gain due to an enhancement of the amount of radiation. To confirm this, we vary L_1 (and hence, pitch), holding the ground plane size $s_x \times s_y$, substrate size $s_{x\text{-}sub} \times s_{y\text{-}sub}$, and antenna size C_{ant} at their reference values: $(s_x \times s_y = s_{x\text{-}sub} \times s_{y\text{-}sub}, C_{ant}, L_1) = (110$ mm $\times$ 110 mm, 240 mm, varied). The analysis reveals that, as L_1 (and hence, pitch) is decreased from 10 mm (leading to M =12 = M_{ref}) to 5 mm (leading to M = 24 = $2M_{ref}$), the gain G_{Lmax} for LH CP radiation in the z-direction increases by 3.3 dB and the gain G_{Rmax} for RH CP radiation in the z-direction increases by 1.1 dB. Note that adjusting the pitch does not lead to a relationship of $G_{Lmax} = G_{Rmax}$ due to the dispersive characteristic of the antenna arm.

The decrease in pitch from 10 mm to 5 mm makes the radiation pattern narrower; the HPBW of the radiation pattern E_L for G_{Lmax} decreases from 82° to 77° in the x-z plane and from 108° to 83° in the y-z plane; the HPBW of the radiation pattern E_R for G_{Rmax} decreases from 40° to 38° in the x-z plane and from 45° to 40° in the y-z plane. It is also found that the decrease in pitch affects the VSWR due to an increase in the number of arm bends (i.e., M–1 arm corners); a $VSWR_{50}$ of less than 2.2, obtained across the overlapping gain and axial-ratio bandwidths O_LBW and O_RBW for a pitch of 10 mm, is deteriorated to 2.7 (at the worst value) for a pitch of 5 mm. Note that, as already mentioned, the axial ratio and gain for the overlapping bandwidths are those calculated in the z-direction.

F. Radiation Squint

The low and high frequencies that let the normalized antenna size be $C_{ant}/\lambda_g = 1$ are defined as f_N and f_H, respectively, in Fig. 6. Similarly, the low and high frequencies that let C_{ant}/λ_g be 2 are newly defined as f_{N2} and f_{H2}, respectively. The first mode radiation occurs at frequencies near f_N and f_H, and the second mode radiation occurs at frequencies near f_{N2} and f_{H2} [16]. As the frequency is decreased from f_N to f_{N2} (*increased from f_H to f_{H2}), the second mode radiation begins to appear and be superimposed onto the first mode radiation. The phases of the second mode radiation with respect to the z-axis have an out-of-phase characteristic, as opposed to those of the first mode radiation (an in-phase characteristic as shown in Figs. 2 and 3). Due to these phase characteristics, the superimposition of the second mode radiation onto the first mode radiation makes the radiation pattern asymmetric with respect to the z-axis, i.e., the radiation squints. This subsection reveals how the pitch and ground plane size effects on the squint.

The effect of the pitch (equals L_1 [mm]) is analyzed using the reference parameters: $(s_x \times s_y = s_{x\text{–}sub} \times s_{y\text{–}sub}, L_1) = (110$ mm $\times$ 110 mm, varied). As in subsection E, the antenna size C_{ant} is held at 240 mm; the cell periodicity p [mm] is changed with a relationship of $p = L_1$ [mm]; and the reactance values are changed to $(p_{ref}/L_1)C_L$ [pF] and $(p_{ref}/L_1)L_L$ [nH].

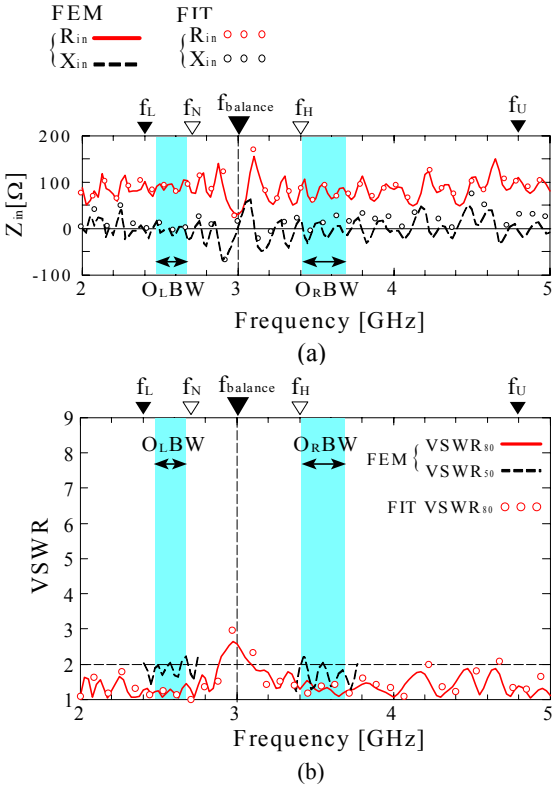

Fig. 11. Frequency response. (a) Input impedance. (b) VSWR relative to a Bloch impedance of 80 ohms ($VSWR_{80}$). VSWRs relative to 50 ohms ($VSWR_{50}$) within the overlapping bandwidths O_LBW and O_RBW are also illustrated.

Table III. COMPARISON

		1-MTM-SPA	2-MTM-SPA
Number of filaments per arm		12	6
Longest filament length		L_{12} = 60 mm	L_6 = 60 mm
Length per arm		420 mm	210 mm
G_{Lmax}		0.92dBi	– 0.56dBi
G_{Rmax}		5.49dBi	4.88dBi
G_LBW		9.6%	14.7%
G_RBW		9.7%	13.6%
AR_LBW		9.0%	3.3%
AR_RBW		8.2%	10.8%
O_LBW		7.0%	3.3%
O_RBW		7.3%	10.8%
VSWR within O_LBW	$VSWR_{50}$	≤2.1	≤2.0
	$VSWR_{80}$	≤1.3	≤1.2
VSWR within O_RBW	$VSWR_{50}$	≤2.2	≤2.2
	$VSWR_{80}$	≤1.5	≤1.4
Radiation efficiency within O_LBW		≤42.2%	≤26.8%
Radiation efficiency within O_RBW		≤24.6%	≤19.4%
Best AR within O_LBW		1.75	2.67
Best AR within O_RBW		0.22	1.16

Fig. 13 shows the radiation patterns at the frequencies for G_{Lmax} and G_{Rmax}. It is found that the beam squints. When the pitch (equals L_1 [mm]) is changed from 10 mm to 5 mm, the squint angle θ_{SQ} (angle θ from the z-axis) of the principal radiation field component E_L at the frequency for G_{Lmax} changes from 5° to 2° in the $\phi = 0°$ plane (x-z plane) and from 6° to −5° in the $\phi = 90°$ plane (y-z plane), while the θ_{SQ} of the E_R at the frequency for G_{Rmax} changes from −6° to −3° in the $\phi = 0°$ plane and from 2° to 0° in the $\phi = 90°$ plane.

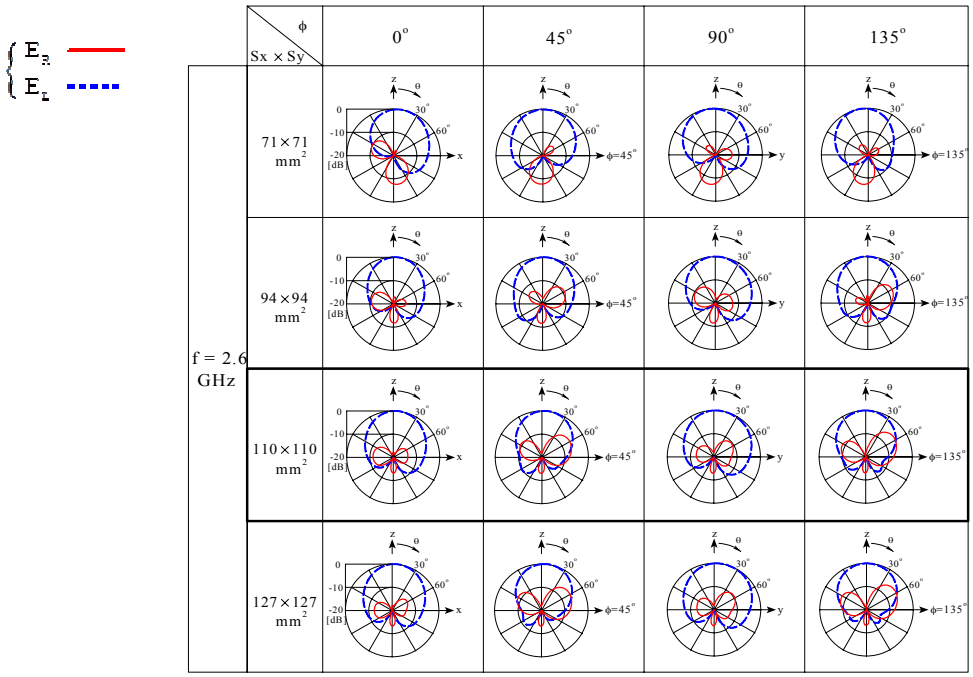

(a)

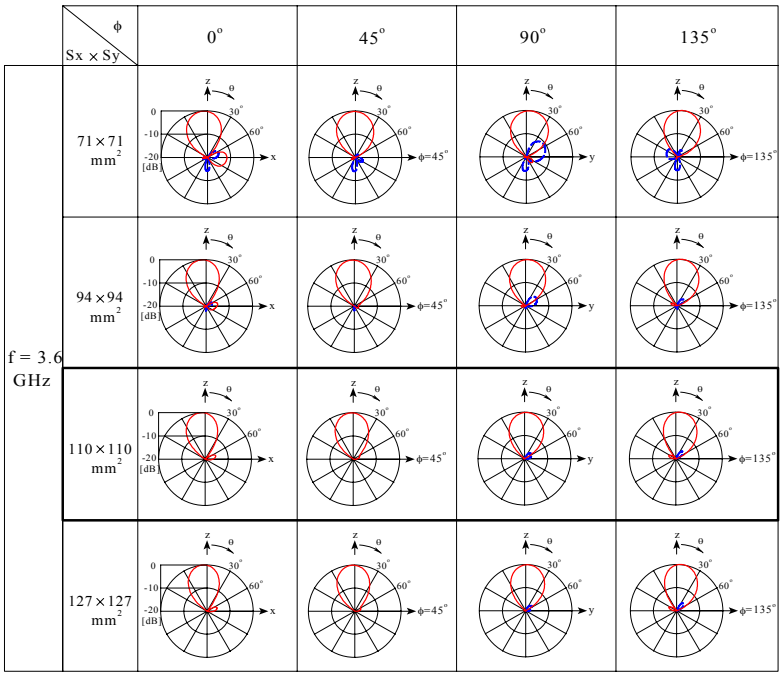

(b)

Fig. 12. Radiation pattern with the $G_{=S}$ ground plane size $s_x \times s_y$ (= $s_{x\text{-sub}} \times s_{y\text{-sub}}$) as a parameter. (a) At 2.6 GHz for LH CP radiation. (b) At 3.6 GHz for RH CP radiation. The parameters except for $s_x \times s_y$ (= $s_{x\text{-sub}} \times s_{y\text{-sub}}$) in Tables I and II are used.

Next, we analyze the effect of the size of a ground plane. The parameters for this analysis are ($s_x \times s_y$, $s_{x-sub} \times s_{y-sub}$, L_1) = (varied, 110 mm × 110 mm, 10 mm), with M_{ref} = 12. Fig. 14 depicts the radiation patterns for LH CP radiation and RH CP radiation, with the ground plane size $s_x \times s_y$ as a parameter, where $s_x \times s_y$ is equal to or larger than the reference value of the substrate size $s_{x-sub-ref} \times s_{y-sub-ref}$ = 110 mm × 110 mm. When the ground plane size $s_x \times s_y$ is changed from 110 mm × 110 mm to 127 mm × 127 mm, the squint angle θ_{SQ} of the principal radiation field component E_L at an LH CP radiation frequency 2.6 GHz changes from 5° to 8° in the ϕ = 0° plane (x-z plane) and from 6° to 15° in the ϕ = 90° plane (y-z plane), while the squint angle θ_{SQ} of the principal radiation field component E_R at an RH CP radiation frequency 3.6 GHz remains unchanged (–6° in the ϕ =0° plane and 2° in the ϕ = 90° plane).

Note that the axial ratio (AR) throughout this paper is the one in the z-direction, not in the squint-beam direction, taking into account practical applications where the radiation in the z-direction is used. It cannot be said that, across the overlapping gain and axial ratio bandwidths O_LBW and O_RBW, the AR in the squint-beam direction is always better than the AR in the z-direction, due to its non-uniform behavior with the frequency. The overall evaluation for the AR across the overlapping bandwidths O_LBW and O_RBW reveals that the ARs in the squint-beam direction and z-direction are almost the same.

VI. Experiment

We designate the 1-MTM-SPA specified by tables I and II as the *original antenna*. Fig. 15 shows an antenna modified from the original antenna. The modified antenna has conducting islands (each having an area of $i_p \times i_w$ = 1.40 mm × 1.65 mm) within apertures (each having an area of $a_p \times a_w$ = 2.00 mm × 2.45 mm) cut in the ground plane, in order to load inductors of L_L. Each inductor is inserted between the island and the ground plane. For this insertion, the pin length in Table I is modified to h_L = 1.6 mm.

First, taking into account the abovementioned structural modification, C_L and L_L in Table I are changed to C_L = 1.30 pF and L_L = 3.00 nH. It is confirmed that the theoretical gain with the changed C_L and L_L shows a relatively good agreement with the gain for the original antenna [G_{Lmax} and G_{Rmax} increase from those for the original antenna only by 0.55 dB and 1.01 dB,

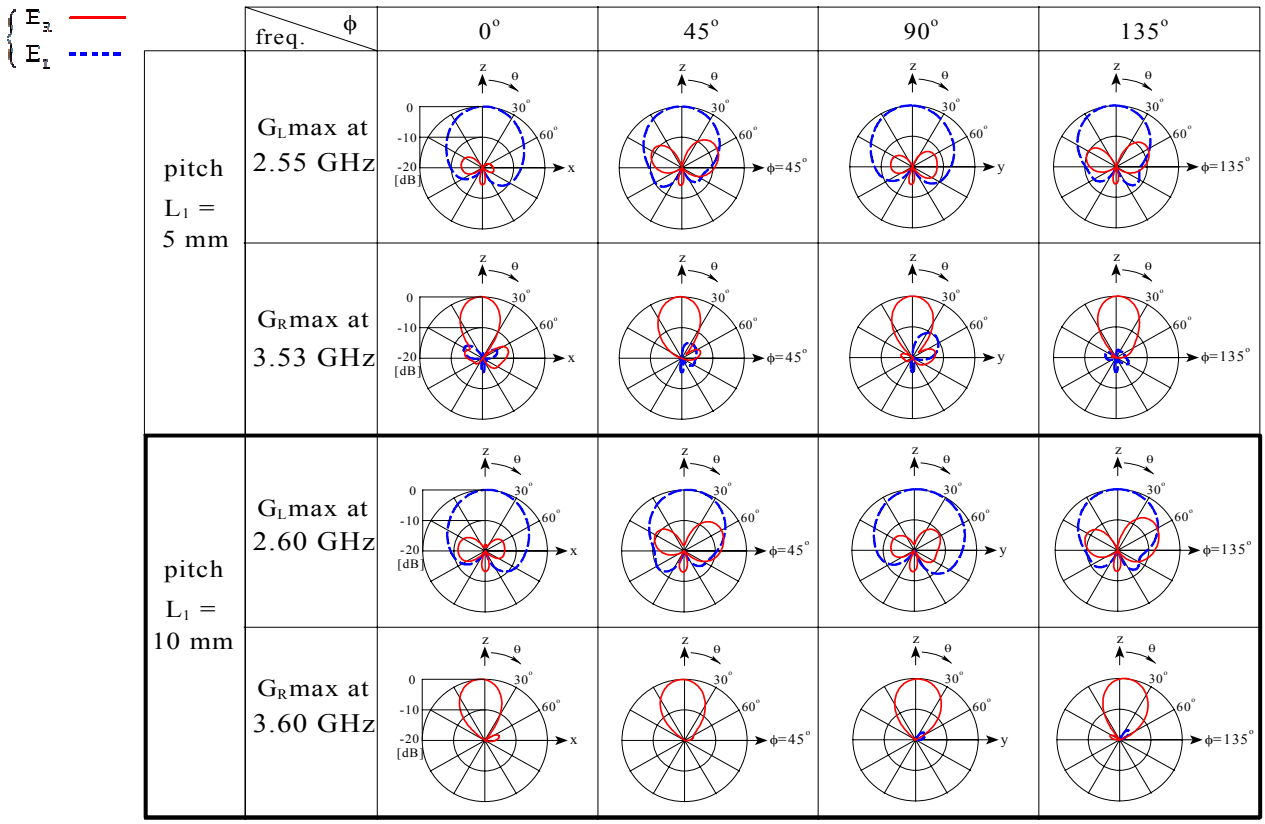

Fig. 13. Radiation patterns for different pitches. The ground plane has the same size as the substrate ($G_{=S}$ ground plane). The parameters are ($s_x \times s_y$ = $s_{x\text{-}sub} \times s_{y\text{-}sub}$, L_1) = (110 mm × 110 mm, varied).

respectively].

Second, we investigate the effect of the losses in the substrate (Teflon of ε_r =2.6 and tan δ = 0.0015) and the conducting material (cupper having a conductivity of 58×10^6 S/m) for the arm, vias, and ground plane. It is revealed that the theoretical gain in this second step decreases from that in the first step only by approximately 0. 3 dB.

Finally, we make an experimental model using 84 commercially available chip capacitors (each having C_L = 1.20 pF, close to 1.30 pF in the first step) and 42 chip inductors (each having L_L = 3.00 nH, the same as the value in the first step). These chip elements have resistive values: approximately 1 ohm for C_L and 0.16 ohm for L_L. In addition, the chip capacitor has an equivalent series lead inductance of 0.43 nH. Figs. 16-18 show the experimental results, including the gain, radiation pattern, and input impedance. The gain and input

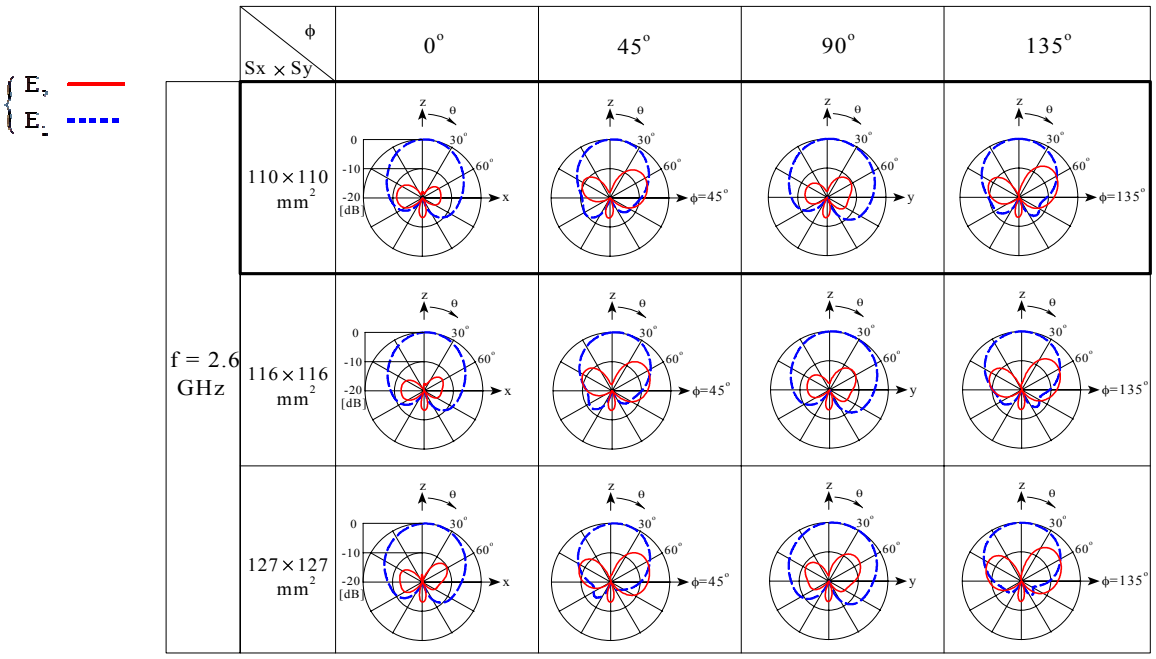

(a)

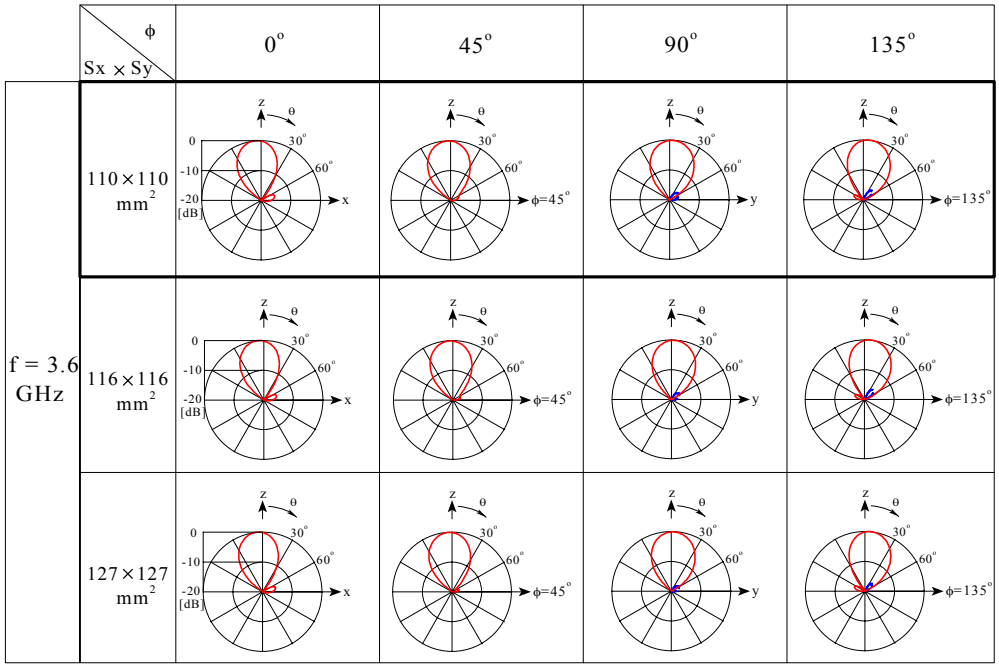

(b)

Fig. 14. Radiation pattern with the ground plane size $s_x \times s_y$ as a parameter. The substrate size is held at its reference value. The parameters are ($s_x \times s_y$, $s_{x\text{-}sub} \times s_{y\text{-}sub}$, L_1) = (varied, 110 mm × 110 mm, 10 mm) with M = 12. (a) At 2.6 GHz for LH CP radiation. (b) At 3.6 GHz for RH CP radiation.

impedance are focused on those across the O_LBW and O_RBW, which are useful/practical frequency bands in the engineering sense. These experimental results are in good agreement with the theoretical results including all losses and lead inductances. Clearly, our goal, i.e., dual-band counter-CP radiation, is confirmed experimentally. Note that the maximum gains G_{Lmax} and G_{Rmax} decrease from those in the first step by approximately 3 dB and 4 dB, respectively, due to the losses in the commercially available material and reactance elements. Development of new reactance elements having a smaller loss will reach the gain in the first step.

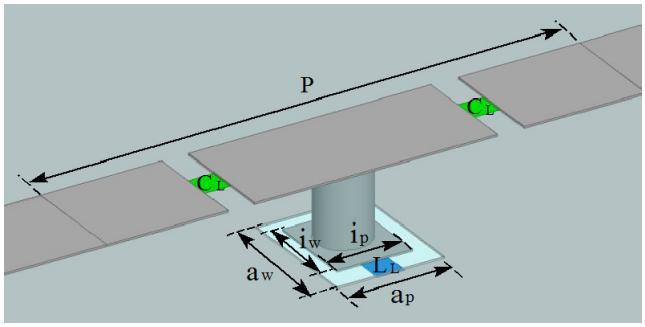

(a)

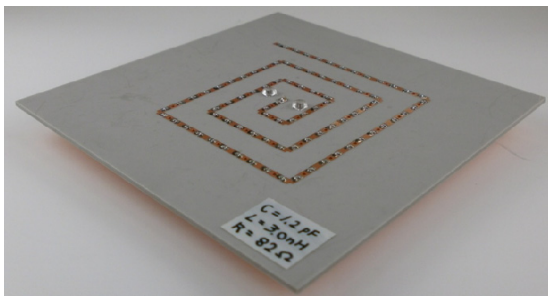

(b)

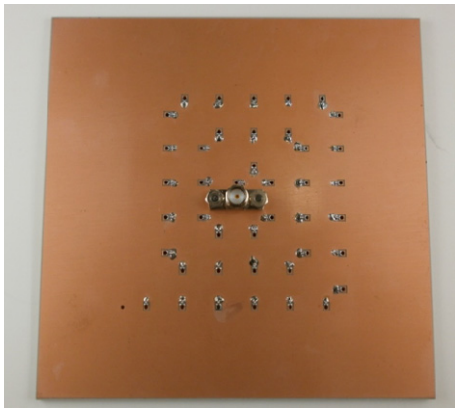

(c)

Fig. 15. Fabricated test antenna. (a) Islands in the ground plane. (b) Perspective view. (c) Reverse side view.

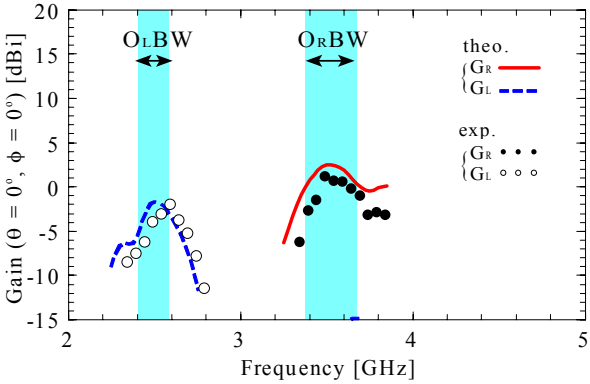

Fig. 16. Experimental and theoretical gains for a lossy structure across the overlapping bandwidths O_LBW and O_RBW.

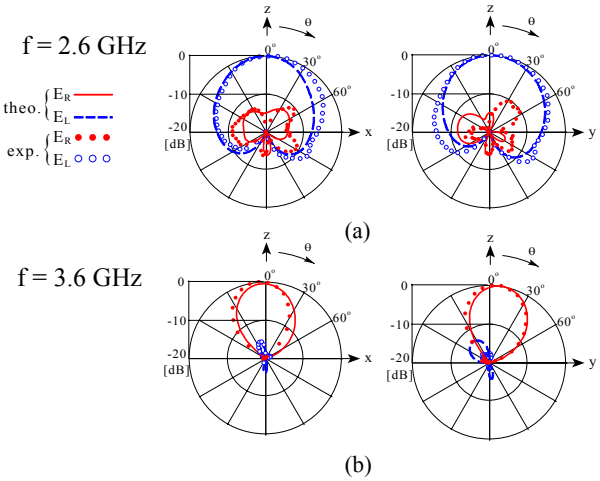

Fig. 17. Experimental and theoretical radiation patterns for a lossy structure. (a) At 2.6 GHz for LH CP radiation. (b) At 3.6 GHz for RH CP radiation.

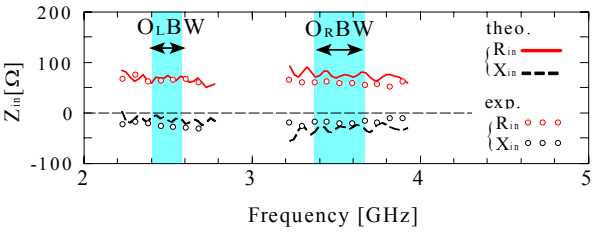

Fig. 18. Experimental and theoretical input impedances for a lossy structure across the overlapping bandwidths O_LBW and O_RBW.

VII. Conclusions

A prediction regarding the existence of dual-band counter-CP radiation is made for a single-arm metamaterial-based spiral antenna (1-MTM-SPA) with inner excitation, where the spiral does not need a balun circuit. To confirm the prediction, a 1-MTM-SPA is designed using a dispersion diagram. Analysis based on two different methods

(FEM and FIT) confirms the prediction of dual-band counter-CP radiation from the behavior of the gain and radiation pattern. The gain for LH CP radiation reaches a maximum near the N frequency f_N, and the gain for RH CP radiation reaches a maximum near the H frequency f_H. The maximum gain for the LH CP radiation is found to be smaller than that for the RH CP radiation, due to a wider HPBW. The overlap of the gain and axial ratio bandwidths is calculated to be moderately wide: 7.0% for the LH CP radiation and 7.3% for the RH CP radiation. The input impedance characteristic is acceptable for practical applications, with a $VSWR_{50}$ of less than 2.2 across the overlapping bandwidths O_LBW and O_RBW. A comparison between the 1-MTM-SPA and the 2-MTM-SPA having the same antenna size reveals that the 1-MTM-SPA has slightly larger radiation efficiency than the 2-MTM-SPA. Note that a fabricated 1-MTM-SPA also confirms the dual-band CP radiation.

ACKNOWLEDGEMENT

We thank V. Shkawrytko for his assistance in the preparation of this manuscript.

REFERENCES

[1] J. A. Kaiser, "The Archimedean two-wire spiral antenna," IRE Trans. Antennas Propagat., vol. 8, no. 3, pp. 312-323, May 1960.
[2] H. Nakano, "Frequency independent antennas," Chap. 6, in *Modern Antenna Handbook*, C. A. Balanis. (Ed), John Wiley & Sons, NJ, 2008.
[3] R. Bawer and J. Wolfe, "A printed circuit balun for use with spiral antennas," IEEE Transactions on MTT, vol. 8, no. 3, pp. 319-325, May 1960.
[4] W-H. Tu and K. Chang, "Wide-band microstrip-to-coplanar stripline/slotline transitions," IEEE Transactions on MTT, vol. 54, no. 3, pp. 1084-1089, March 2006.
[5] M. Haneishi, K. Hirasawa, and Y. Suzuki, *Small planar antenna,* in Japanese, IEICE, Tokyo, 1996.
[6] H. Nakano, J. Miyake, M. Oyama, and J. Yamauchi, "Metamaterial spiral antenna," IEEE AWPL, vol. 10, pp. 1555-1558, 2011.
[7] G. Eleftheriades and K. Balmain, *Negative-refraction metamaterials: fundamental principles and applications*, Wiely, NJ, 2005.
[8] C. Caloz and T. Itoh, *Electromagnetic Metamaterials,* Wiley, NJ, 2006.
[9] N. Engheta and R. Ziolkowski (editors), *Metamaterials*, Wiley, NJ, 2006.
[10] Mushiake, *Self-complementary antennas*, Springer, NY, 1996.
[11] V. H. Rumsey, *Frequency Independent Antennas*, Academic Press, NY, 1966.
[12] HFSS. ANSYS, Canonsburg, PA, 2011 [Online]. Available: http://www.ansoft.com/products/hf/hfss
[13] CST-MWS. ver. 13, Computer Simulation Technology, Framingham, MA, 2011 [Online]. Available: http://www.cst.com/Content/Products/MWS/Overview.aspx
[14] R. Collin, *Foundation for microwave engineering*, McGraw Hill, Tokyo, 1966.
[15] H. Nakano, J. Eto, Y. Okabe, and J. Yamauchi, "Tilted- and axial-beam formation by a single-arm rectangular spiral antenna with compact dielectric substrate and conducting plane," IEEE Trans. Antennas Propagat., vol. 50, no. 1, pp. 17-24, January 2002.
[16] H. Nakano, Y. Shinma, and J. Yamauchi, "A monofilar spiral antenna and its array above a ground plane-formation of a circularly polarized tilted fan beam," IEEE Trans. Antennas and Propagat., vol. 45, no. 10, pp. 1506-1511, October 1997.

Hisamatsu Nakano (M'75-SM'87-F'92-LF'11) received his Dr. E. degrees in electrical engineering from Hosei University, Tokyo, in 1974. Since 1973, he has been a member of the faculty of Hosei University, where he is now a Professor at the Electrical and Electronics Engineering Department. His research topics include numerical methods for low- and high-frequency antennas and optical waveguides. He received the IEE (currently IET) International Conference on Antennas and Propagation Best Paper Award and the IEEE Transactions on Antennas and Propagation Best Application Paper Award (H. A. Wheeler Award) in 1989 and 1994, respectively. In 1992, he was elected an IEEE fellow for contributions to the design of spiral and helical antennas. He was also the recipient of the Chen-To Tai Distinguished Educator Award (from the IEEE Antennas and Propagation Society) in 2006 and the recipient of the Prize for Science and Technology (from Japan's Minister of Education, Culture, Sports, Science, and Technology) in 2010. Prof. Nakano is an associate editor of several journals and magazines, such as Electromagnetics, IEEE Antennas and Propagation Society Magazine, IEEE Antennas and Wireless Propagation Letters.

Junya Miyake was born in Tokyo, Japan, on October 2, 1988. He is currently working toward the M.E. degree in electronic informatics from Hosei University, Tokyo, Japan.

Mr. Miyake is a Member of the Institute of Electronics, Information and Communication Engineers (IEICE) of Japan.

Tomoki Sakurada was born in Saitama, Japan, on August 30, 1988. He is currently working toward the M.E. degree in electronic informatics from Hosei University, Tokyo, Japan.

Mr. Sakurada is a Member of the Institute of Electronics, Information and Communication Engineers (IEICE) of Japan.

Junji Yamauchi (M'84-SM'08-F'12) was born in Nagoya, Japan, on August 23, 1953. He received the B. E., M. E., and Dr. E. degrees from Hosei University, Tokyo, Japan, in 1976, 1978, and 1982, respectively. From 1984 to 1988, he served as a Lecturer in the Electrical Engineering Department of Tokyo Metropolitan Technical College. Since 1988, he has been a member of the faculty of Hosei University, where he is now a Professor at the Electrical and Electronics Engineering Department. His research interests include optical waveguides and circularly polarized antennas. He is the author of Propagating Beam Analysis of Optical Waveguides (Baldock, Hertfordshire, U.K.: Research Studies Press, 2003). Dr. Yamauchi is a member of the Optical Society of America and the Institute of Electronics, Information and Communication Engineers (IEICE) of Japan.